

CRAM: Centroid-Routing and Adaptive MoE for Multimodal Continual Instruction Tuning

Jun-Tao Tang^{* 2}, Zhen-Hao Xie^{* 1,2}, Yu-Cheng Shi², Da-Wei Zhou^{1,2,†}

¹ School of Artificial Intelligence, Nanjing University, China

² State Key Laboratory of Novel Software Technology, Nanjing University, China

^{*} Equal contribution [†] Corresponding Author

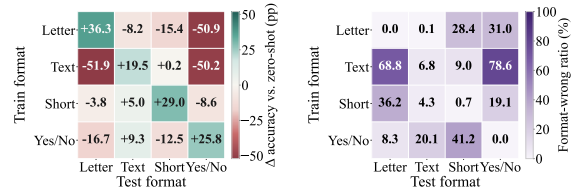
{juntao.tang, 231250034}@smail.nju.edu.cn, {wenzh, zhoudw}@lamda.nju.edu.cn

Abstract

Multimodal Large Language Models (MLLMs) unify heterogeneous vision-language tasks under a shared generative framework via instruction tuning, yet real-world deployment demands continuous capability expansion, making Multimodal Continual Instruction Tuning (MCIT) essential. Existing methods either update all tasks with a shared parameter set or allocate dedicated modules for each new task. Shared updates force heterogeneous tasks to compete, causing forgetting of learned capabilities. Conversely, isolated expansion prevents interference but severely limits parameter efficiency over long task streams. To address this dilemma, we propose CRAM (Centroid Routing Adaptive MoE). Specifically, by isolating task-specific patterns into independent modules, CRAM mitigates catastrophic forgetting across tasks. To further boost parameter efficiency, we utilize adaptive-rank instantiation to identify the capability gap between existing expert capability and new task demands, and dynamically allocate only the necessary parameters. To ensure stable reuse among tasks, centroid-guided routing recognizes and activates existing experts' capabilities, while an orthogonality penalty confines new updates to task-specific directions, preventing re-learning general capability. Extensive experiments across diverse benchmarks consistently demonstrate its superiority over existing methods.

1 Introduction

Recently, multimodal Large Language Models (MLLMs) (Bai et al., 2023; Liu et al., 2023; Zhu et al., 2023) have achieved remarkable capabilities through multimodal instruction tuning (Zhang et al., 2023a; Tong et al., 2025; Che et al., 2026). By reformulating heterogeneous vision-language problems into a unified generative framework, instruction tuning enables MLLMs to generalize across diverse downstream applications (Tu et al.,



(a) Change vs. Zero-shot (b) Format-wrong ratio

Figure 1: Format-level interference. (a) Accuracy change relative to zero-shot for each train-test format pair. (b) Ratio of format wrong but semantically correct responses among errors.

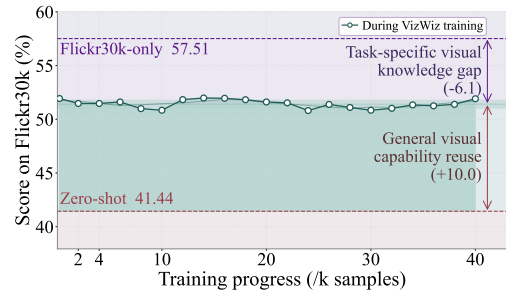


Figure 2: Transfer on Flickr30k during VizWiz training.

2025; Guo et al., 2025c; Kim et al., 2026), from visual reasoning to document understanding. While standard MLLM optimization relies on a static multitask regime that assumes joint data availability (Liu et al., 2023; Jiang et al., 2026), real-world deployment rarely satisfies this premise: tasks arrive sequentially, inherently introducing distribution shifts across both instructional formats and visual domains. As a result, a practically useful MLLM must continually acquire new capabilities, yet sequential adaptation inherently risks catastrophic forgetting (Zhou et al., 2024a; Kirkpatrick et al., 2017; Rebuffi et al., 2017; Ge et al., 2025), where gradient updates for new tasks overwrite established representations and degrade historical performance. To enable continuous capability acquisition while mitigating this degradation, multimodal continual instruction tuning (MCIT) (Chen et al., 2024; Huo and Tang, 2025; Qiao et al., 2024)

has emerged as a critical paradigm.

Existing MCIT methods mainly consider shared adaptation or parameter isolation. Shared approaches (Chen et al., 2025; Marouf et al., 2025; Wang et al., 2025c) update all tasks within a single parameter set, causing new updates to overwrite learned patterns. Conversely, isolation methods (Guo et al., 2025b; Jia et al., 2025) assign separate modules to each task, leading to unbounded parameter growth and preventing general ability from being shared across tasks. Nevertheless, they overlook a key balance: task-specific patterns must be isolated to avoid interference, while general knowledge should be preserved for reuse.

To identify what requires isolation and what can be shared, we design controlled experiments that fix one modality while varying the other. First, to isolate the impact of instruction formats, we use the ArxivQA (Li et al., 2024) dataset to generate four response variants by altering the instruction-response convention. For example, we convert a multiple-choice question into a short-answer format by extracting the correct option’s content and adjusting the prompt accordingly (see Appendix B for details). We then fine-tune the model on one variant and evaluate it across the others. As shown in Fig. 1a, training on any single format severely degrades performance on the rest: the model generates semantically accurate answers but fails to adhere to the required output conventions (Fig. 1b). This confirms that heterogeneous instruction formats inherently trigger severe interference, acting as a primary factor of catastrophic forgetting in shared-parameter regimes.

We further examine how visual representations behave across distinct domains. Specifically, we select two datasets with the same answer format but non-overlapping visual content: VizWiz (Gurari et al., 2018) and Flickr30k (Plummer et al., 2015). Throughout the training process on VizWiz, we monitor the model’s performance on Flickr30k. As shown in Fig. 2, the accuracy stabilizes above the zero-shot baseline but remains below direct fine-tuning on Flickr30k. These results confirm that visual capabilities are partly transferable across tasks, while task-specific ability learning remains necessary. Critically, this reveals a fundamental limitation of isolation methods: by segregating tasks into independent modules, it inherently blocks the reuse of transferable capabilities, forcing redundant learning and limiting parameter efficiency.

Collectively, these findings demonstrate that

instruction conventions are highly sensitive patterns requiring isolation, whereas visual capabilities are partially transferable and thus can be reused. Guided by this insight, we propose CRAM (Centroid Routing Adaptive MoE). It groups instructions by similarity into separate clusters, isolating conflicting updates to prevent format interference. Within each cluster, adaptive-rank instantiation filters out directions already mastered by historical experts, allocating parameters strictly to unmet capability gaps, naturally bounding model growth. Centroid-guided routing further stabilizes expert reuse by directing inputs to experts with aligned capabilities, while an orthogonality penalty confines new updates to missing patterns, preventing them from overwriting historical knowledge. Together, CRAM achieves state-of-the-art performance by balancing format isolation with visual reuse, without compromising parameter efficiency.

2 Related Work

Continual instruction tuning (Chen et al., 2024; Roth et al., 2024; Jin et al., 2025) is essential for deploying MLLMs in open-world settings (Liu et al., 2025b). Existing methods predominantly adopt one of two structural paradigms: *shared adaptation* consolidates trainable parameters into a unified subspace (e.g., LoRA/MoE-LoRA) to maximize plasticity, often supplemented by replay (Li et al., 2025; Lee et al., 2025; Yu et al., 2025) or regularization (Zeng et al., 2025; Liu et al., 2025a), yet inevitably entangles heterogeneous instruction patterns and triggers gradient interference (Wang et al., 2023; Cao et al., 2024); *parameter isolation* mitigates interference by allocating task-dedicated modules (Huai et al., 2025; Wang et al., 2025a; Yu et al., 2025), preserving stability but fracturing reusable visual competencies and incurring linear parameter growth. Despite their divergent implementations, both paradigms frame sharing and isolation as mutually exclusive. This overlooks the heterogeneous structure of multimodal knowledge (Marouf et al., 2025), where some instructional patterns require isolation while transferable visual representations should be systematically reused (Zhao et al., 2025; Wang et al., 2025b).

3 Preliminaries

Multimodal Continual Instruction Tuning (MCIT). We consider an MLLM (Liu et al., 2023) comprising a vision encoder $\phi(\cdot)$, a multimodal

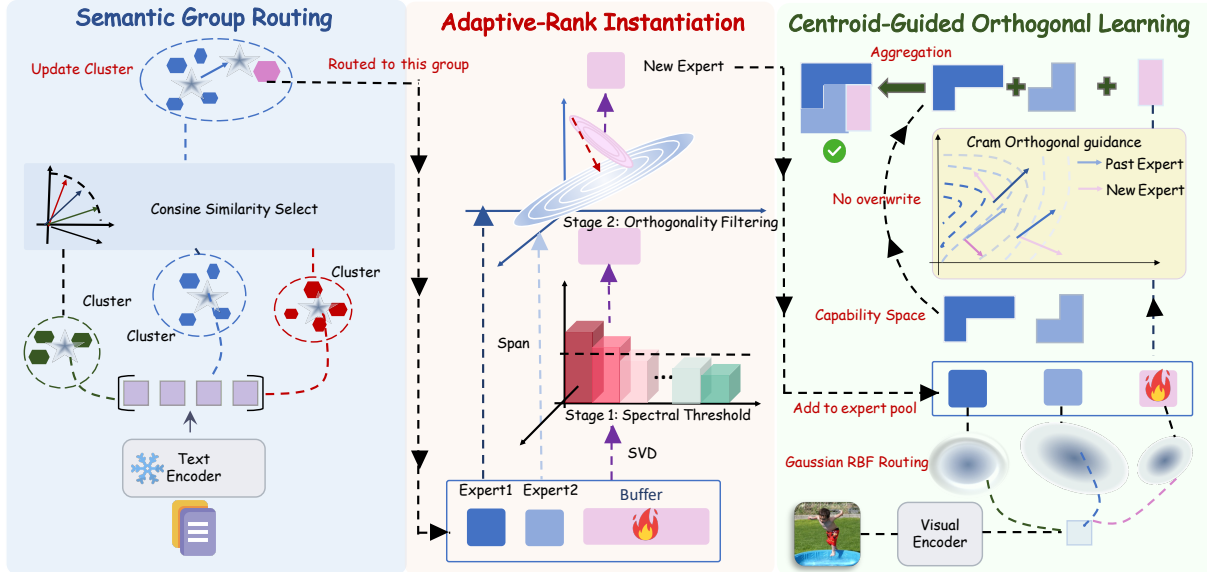


Figure 3: Overview of CRAM. CRAM decouples via (i) *Semantic Group Routing* that group instructions with semantic similarity to protect output conventions, (ii) *Adaptive-Rank Instantiation* that allocates parameters exclusively to capability gaps via orthogonality filtering, and (iii) *Centroid-Guided Orthogonal Learning* to stabilize expert activation while confining new updates to orthogonal subspaces.

projector $\pi(\cdot)$, and an LLM backbone $f(\cdot)$. To enable continual adaptation (Chen et al., 2024; Wang et al., 2025a), we inject lightweight modules into the LLM (Zhu et al., 2025), with trainable parameters denoted as θ . Let $\{\mathcal{D}_t\}_{t=1}^T$ denote a sequential task stream, where $\mathcal{D}_t = \{(v_i, q_i, y_i)\}_{i=1}^{n_t}$ contains images v_i , instructions q_i , and response sequences $y_i = (y_{i,1}, \dots, y_{i,L_i})$. Each input is encoded as $z_i = [\pi(\phi(v_i)); \text{Emb}(q_i)]$, where $\text{Emb}(\cdot)$ is the token embedding layer of f . The model generates responses autoregressively, factorizing the conditional probability as $p_\theta(y_i | z_i) = \prod_{j=1}^{L_i} p_\theta(y_{i,j} | z_i, y_{i,<j})$. The negative log-likelihood loss is defined as:

$$\mathcal{L}_{\text{NLL}} = - \sum_{j=1}^{L_i} \log p_\theta(y_{i,j} | z_i, y_{i,<j}). \quad (1)$$

The learning objective at task t is formulated as:

$$\theta_t^* = \arg \min_{\theta} \mathbb{E}_{(v_i, q_i, y_i) \sim \mathcal{D}_{\leq t}} [\mathcal{L}_{\text{NLL}}(\theta; z_i, y_i)],$$

where $\mathcal{D}_{\leq t} = \bigcup_{k=1}^t \mathcal{D}_k$ denotes all data observed up to task t . In rehearsal-free MCIT setting (Chen et al., 2024; Xie et al., 2026), we can only access \mathcal{D}_t when learning task t . This mismatch between the global cumulative objective and the locally available data inherently drives catastrophic forgetting. **MoE with LoRA Experts.** In conventional MoE-LoRA designs, the backbone remains frozen while a pool of trainable LoRA experts is injected into specific modules (Liu et al., 2025b; Zhu et al.,

2025). Let \mathbf{W}_0 denote the frozen weight and $\Delta \mathbf{W}_i = \mathbf{B}_i \mathbf{A}_i$ be the low-rank update for the i -th expert. Given an input $h \in \mathbb{R}^d$ at a layer, the layer output is computed as:

$$h' = \mathbf{W}_0 h + \sum_{i=1}^N \omega_i \Delta \mathbf{W}_i h = \mathbf{W}_0 h + \sum_{i=1}^N \omega_i \mathbf{B}_i \mathbf{A}_i h,$$

where $\omega_i = \text{Softmax}_\tau(\mathbf{W}_G h)_i$ denotes the routing weight for expert i . Here, $\mathbf{W}_G \in \mathbb{R}^{N \times d}$ is the linear gating matrix and τ is the temperature.

Discussion. While effective in static environments, the linear gating degrades under continual instruction tuning with multiple tasks, since a single router is forced to simultaneously satisfy conflicting format isolation and visual reuse objectives.

4 Method

To address the isolation-sharing dilemma, we follow a straightforward intuition: by isolating conflicting instruction formats first, we can safely reuse general ability and focus parameter allocation solely on the specific gaps that truly need them.

4.1 Group-Isolated Semantic Routing

In a continual instruction stream, tasks arrive sequentially with heterogeneous formats. Under the shared adaptation paradigm, unified optimization entangles gradient flows, triggering instruction-level interference. Resolving this requires grouping instructions by semantic intent, isolating conflicting updates to prevent cross-format interference.

To implement this, we employ a frozen CLIP (Radford et al., 2021) text encoder $\psi(\cdot)$ to extract instruction embeddings, yielding normalized vectors $\mathbf{e}(q) = \psi(q)/\|\psi(q)\|_2$. We maintain a cluster center \mathbf{c}_g for each semantic group by averaging the instruction embeddings $\mathbf{e}(q)$ routed to it, while tracking the corresponding sample count n_g . Semantic affinity to that group is subsequently measured via cosine similarity $s_g(q) = \frac{\mathbf{c}_g^\top \mathbf{e}(q)}{\|\mathbf{c}_g\|_2}$.

Absolute similarity scores fluctuate unpredictably under distribution shifts. We instead adopt a relative confidence margin. Let $s_{(1)}(q)$ and $s_{(2)}(q)$ denote the highest and second-highest cosine similarities. The assignment margin is:

$$\Delta(q) = s_{(1)}(q) - s_{(2)}(q). \quad (2)$$

If $\Delta(q) > \theta$, q is confidently assigned to the best-matching cluster $g^* = g_{(1)}$; otherwise, we instantiate a new center $\mathbf{c}_{\text{new}} \leftarrow \mathbf{e}(q)$. Then, the matched cluster’s center is updated via:

$$\mathbf{c}_{g^*} \leftarrow \frac{n_{g^*} \mathbf{c}_{g^*} + \mathbf{e}(q)}{n_{g^*} + 1}, \quad n_{g^*} \leftarrow n_{g^*} + 1. \quad (3)$$

This applies a diminishing step size that naturally attenuates transient noise as clusters expand, ensuring routing boundaries evolve smoothly. By grouping instructions with semantic similarity, we protect output conventions, enabling the ability to be safely reused within groups.

4.2 Adaptive-Rank Expert Instantiation

As new tasks arrive continuously, allocating fixed-size experts for each task induces unbounded parameter expansion, whereas allocating no additional experts causes existing parameters to be overwritten, triggering catastrophic forgetting. Fig. 2 reveals that most visual capabilities required by new tasks are largely covered by existing experts, leaving only a small capability gap. Motivated by this, we argue that parameter allocation should exclusively target this gap, reframing the core challenge as dynamically determining the minimal capacity required to encode incremental task knowledge.

To probe the capability gaps, we introduce a warm-up phase that accumulates initial gradient updates into a temporary LoRA buffer \mathbf{W}_B . As the raw update $\Delta \mathbf{W}_B$ mixes task-specific signals with shared gradient components, we apply Singular Value Decomposition to isolate the principal

directions that capture the unmet capability gaps:

$$\Delta \mathbf{W}_B = \sum_{p=1}^P \sigma_p \mathbf{u}_p \mathbf{v}_p^\top, \quad \sigma_1 \geq \dots \geq \sigma_P. \quad (4)$$

This spectral representation explicitly ranks directional components by geometric significance. To identify the novel correction signals, we implement a two-stage geometric filtering pipeline:

(1) *Spectral Thresholding*: Directions with $\sigma_p \leq \tau_{\text{alloc}}$ are discarded to filter optimization noise, yielding the candidate set \mathcal{C} .

(2) *Historical Subspace Orthogonality Filtering*: In group g^* , to prevent allocating parameters to already mastered subspaces, we quantify each candidate’s novelty against the expert pool \mathcal{E}_{g^*} . Since the rows of each down-projection matrix \mathbf{A}_i span the input directions actively modified by expert i , we horizontally concatenate their transposes to characterize the union of previously optimized subspaces, yielding the unified historical representation:

$$\mathbf{M}_{\text{hist}} = [\mathbf{A}_1^\top, \dots, \mathbf{A}_{|\mathcal{E}_{g^*}|}^\top] \in \mathbb{R}^{d \times R_{\text{hist}}}, \quad (5)$$

where $R_{\text{hist}} = \sum_{i=1}^{|\mathcal{E}_{g^*}|} \text{rank}(\mathbf{A}_i)$. We then extract an orthonormal basis \mathbf{Q} for $\text{col}(\mathbf{M}_{\text{hist}})$ via QR decomposition (Ye and Li, 2005). Geometrically, $\mathbf{Q}\mathbf{Q}^\top$ acts as an orthogonal projector onto the historical subspace. By applying the complementary operator $(\mathbf{I} - \mathbf{Q}\mathbf{Q}^\top)$ to each candidate direction $\mathbf{v}_p \in \mathcal{C}$, we isolate the component orthogonal to established directions. The magnitude of this residual quantifies geometric independence, reflecting the novel optimization capacity \mathbf{v}_p introduces. To eliminate scale dependence, we normalize this by $\|\mathbf{v}_p\|_2$, yielding a bounded orthogonality score:

$$\alpha_p = \frac{\|(\mathbf{I} - \mathbf{Q}\mathbf{Q}^\top)\mathbf{v}_p\|_2}{\|\mathbf{v}_p\|_2}. \quad (6)$$

Only directions satisfying $\alpha_p > \tau_{\text{orth}}$ are retained in \mathcal{S} to reconstruct the final expert parameters:

$$\mathbf{A}_t = \Sigma_{\mathcal{S}}^{1/2} \tilde{\mathbf{V}}_{\mathcal{S}}^\top, \quad \mathbf{B}_t = \mathbf{U}_{\mathcal{S}} \Sigma_{\mathcal{S}}^{1/2}, \quad (7)$$

where $\mathbf{U}_{\mathcal{S}}$ and $\tilde{\mathbf{V}}_{\mathcal{S}}$ denote the retained singular vectors, and $\Sigma_{\mathcal{S}}$ their corresponding singular values. By filtering out directions already covered by historical experts, we only allocate parameters to capability gaps, bounding model growth while preserving established representations.

4.3 Centroid-Guided Orthogonal Learning

With experts instantiated, another problem arises: how to achieve stable intra-group reuse? Unlike conventional MoE with a static expert pool, MCIT must continuously expand the pool as tasks arrive. This introduces two bottlenecks: First, continuous updates to routing matrices induce boundary drift, creating a training-inference mismatch in expert activation. Second, optimization of subsequent experts within a shared parameter space compounds overlapping feature directions. As the pool expands, repeated updates inflate the magnitude of these directions, skewing MoE aggregation and suppressing novel corrections.

To address these challenges, we assign a dedicated learnable centroid $\mathbf{w}_k \in \mathbb{R}^{d_v}$ to each expert, collectively forming $\mathcal{W} = \{\mathbf{w}_k\}$. These centroids act as geometric anchors that directly govern expert activation. Upon task completion, each centroid is permanently frozen to lock its decision boundary against future shifts. For an incoming visual input v_i , we extract its aggregated representation via the MLLM’s frozen vision encoder $\phi(\cdot)$ as $\boldsymbol{\xi}_i = \text{MeanPool}(\phi(v_i)) \in \mathbb{R}^{d_v}$. The routing function ρ then computes a proximity score $\rho_{i,k} = \rho(\boldsymbol{\xi}_i, \mathbf{w}_k)$ for every centroid. Within group g^* , these scores are normalized across the expert pool \mathcal{K}_{g^*} to yield the routing weights:

$$\omega_{i,k} = \frac{\rho_{i,k}}{\sum_{j \in \mathcal{K}_{g^*}} \rho_{i,j}}, \quad \forall k \in \mathcal{K}_{g^*}. \quad (8)$$

Balancing historical reuse with novel learning requires the routing function to maintain high activation for queries near known centroids while smoothly decaying for distant ones. We achieve this via a Gaussian radial basis kernel:

$$\rho(\boldsymbol{\xi}_i, \mathbf{w}_k) = \exp\left(-\frac{\|\boldsymbol{\xi}_i - \mathbf{w}_k\|_2^2}{2\sigma^2}\right), \quad (9)$$

where σ controls the bandwidth.

Besides the routing function, proper initialization is also critical. Naive random or zero initialization places centroids off the data manifold, triggering routing collapse. Instead, for a centroid \mathbf{w}_k , we anchor it within the local data distribution: during the warm-up phase (Sec. 4.2), \mathbf{w}_k is initialized as the mean of its corresponding accumulated queries $\boldsymbol{\xi}$. After the warm-up, the centroid is updated via backpropagation for continuous adaptation.

Despite stabilized routing, a structural imbalance persists in expert aggregation. As new experts

are instantiated, their updates inherently contain directions shared with historical experts. While new experts learn to cooperate with the existing expert pool during training, historical experts have never adapted to co-activate with future ones. During inference, when an input simultaneously activates both historical and new experts, their outputs along shared directions sum without coordination, causing the effective magnitude of these redundant components to accumulate disproportionately. In contrast, task-specific directions are encoded by a single expert and remain comparatively small. This magnitude imbalance skews the aggregated MoE output toward redundant features, suppressing novel correction signals. To restore balance, new updates must exclusively target unrepresented residuals. We thus constrain $\Delta \mathbf{W}_{\text{new}}$ to the orthogonal complement of historical subspaces. Using the precomputed \mathbf{Q} (Sec. 4.2), we enforce this via an orthogonality penalty for a batch of size B :

$$\mathcal{L}_{\text{dec}} = \frac{1}{B} \sum_{i=1}^B \gamma_i \cdot \|\Delta \mathbf{W}_{\text{new}} (\mathbf{Q} \mathbf{Q}^\top \mathbf{h}_i)\|_2^2, \quad (10)$$

where $\gamma_i = \sum_{k \in \mathcal{K}_{g^*}} \omega_{i,k}$ measures reliance on historical experts, and \mathbf{h}_i denotes input hidden states.

Discussion. By routing via visual affinity to stable centroids, we stabilize expert reuse, while an orthogonality penalty guides new updates to unlearned directions, ensuring clean aggregation and learning only what is truly needed.

4.4 Summary of CRAM

For each task, CRAM executes a pipeline: a warm-up phase first accumulates visual queries to initialize centroids \mathcal{W} and extract the historical basis \mathbf{Q} , guiding data-driven expert instantiation (Eq. 7). During optimization, centroid-guided routing (Eqs. 8–9) stabilizes capability reuse, while a penalty (Eq. 10) constrains new updates to orthogonal subspaces. Building upon the standard generation loss (Eq. 1), the joint objective is:

$$\mathcal{L} = \mathcal{L}_{\text{NLL}} + \mathcal{L}_{\text{dec}}. \quad (11)$$

Upon convergence, historical experts and centroids are frozen before starting the next task. During inference, routing weights are computed directly via Eq. 8. The algorithm is detailed in Appendix A.

Table 1: Performance on UCIT. The best and second-best results are highlighted in **bold** and underline, respectively.

Methods	ImageNet-R	ArxivQA	Vizcap	IconQA	CLEVR	Flickr30k	Average
Zero-shot (Liu et al., 2023)	18.88	52.62	38.75	21.25	21.12	41.44	32.34
FT-LoRA (Hu et al., 2022)	29.33	55.30	45.51	26.13	13.07	58.07	37.90
MoE-LoRA (Chen et al., 2024)	58.43	77.57	44.83	68.90	56.73	58.27	60.79
Replay-LoRA	76.93	87.07	54.31	56.43	36.40	55.94	61.18
CL-MoE (Huai et al., 2025)	64.12	78.38	44.83	62.00	50.75	58.06	59.69
HiDe-LLaVA (Guo et al., 2025a)	87.62	91.12	42.68	57.62	31.00	50.41	60.08
ModalPrompt (Zeng et al., 2025)	80.50	90.62	<u>60.13</u>	63.50	55.75	57.09	67.93
DISCO (Guo et al., 2025b)	88.88	94.25	47.52	69.50	60.75	56.32	69.54
SAME (Xie et al., 2026)	89.91	91.40	55.33	<u>77.51</u>	68.85	55.43	<u>73.07</u>
CRAM (Ours)	87.23	<u>92.17</u>	60.55	80.43	70.67	57.35	74.73

Table 2: Performance on TriGap. The best and second-best results are highlighted in **bold** and underline, respectively.

Methods	PMCVQA	DocVQA	ChartQA	IconQA	InfographicVQA	ArxivQA	Roadside	ChemVQA	FloodNetVQA	CLEVR	Average
Zero-shot (Liu et al., 2023)	35.40	12.68	9.36	19.27	5.06	53.77	7.40	5.30	47.41	20.37	21.60
FT-LoRA (Hu et al., 2022)	34.20	23.32	9.84	37.07	23.53	83.83	7.00	12.70	80.31	60.27	37.21
Replay-LoRA	33.70	33.95	14.00	46.67	28.97	75.57	9.40	15.90	73.81	58.80	39.08
MoE-LoRA (Chen et al., 2024)	39.03	37.49	12.44	43.43	35.17	90.90	7.93	20.70	90.41	67.00	44.45
HiDe-LLaVA (Guo et al., 2025a)	37.00	33.20	10.52	41.97	24.09	79.20	7.73	11.17	57.39	23.00	32.53
ModalPrompt (Zeng et al., 2025)	38.23	38.23	11.92	44.73	37.37	84.47	10.13	12.43	71.52	52.50	40.15
CL-MoE (Huai et al., 2025)	40.53	36.79	13.72	52.70	32.27	93.00	7.77	18.33	80.09	<u>65.90</u>	44.11
SAME (Xie et al., 2026)	41.60	<u>43.87</u>	<u>17.56</u>	<u>64.03</u>	39.57	90.46	<u>10.83</u>	21.77	<u>81.09</u>	54.50	46.53
DISCO (Guo et al., 2025b)	<u>42.03</u>	43.50	18.01	63.13	38.23	91.27	<u>11.02</u>	<u>22.13</u>	80.25	55.87	<u>46.54</u>
CRAM (Ours)	43.60	44.33	16.92	66.00	<u>39.17</u>	<u>91.83</u>	12.83	24.27	79.49	59.53	47.79

5 Experiment

5.1 Implementation Details

Datasets. We evaluate CRAM on two widely used benchmarks. **UCIT** (Guo et al., 2025a) comprises six tasks: ArxivQA (Li et al., 2024), CLEVR-Math (Lindström and Abraham, 2022), IconQA (Lu et al., 2021), ImageNet-R (Hendrycks et al., 2021), VizWiz-Caption (Gurari et al., 2018), and Flickr30k (Plummer et al., 2015). **TriGap** (Xie et al., 2026) encompasses ten tasks: PMCVQA (Zhang et al., 2023b), DocVQA (Mathew et al., 2021), ChartQA (Masry et al., 2022), IconQA (Lu et al., 2021), InfographicVQA (Mathew et al., 2022), ArxivQA (Li et al., 2024), Roadside (Guan et al., 2026), ChemVQA (Sabando et al., 2020), FloodNetVQA (Rahnemoonfar et al., 2021), and CLEVR-Math (Lindström and Abraham, 2022).

Compared Methods. We compare CRAM with state-of-the-art MCIT approaches, encompassing two representative structural paradigms: (1) *Shared adaptation*: including FT-LoRA, Replay-LoRA, MoE-LoRA (Chen et al., 2024), CLMoE (Huai et al., 2025), and SAME (Xie et al., 2026); and (2) *Parameter isolation*: including HiDe-LLaVA (Guo et al., 2025a), DISCO (Guo et al., 2025b), and ModalPrompt (Zeng et al., 2025). We additionally report Zero-shot (Liu et al., 2023) performance as a lower-bound reference. To ensure a fair comparison, all methods adhere to identical backbone architectures and data protocols.

Training Details. All experiments are conducted on 4 NVIDIA RTX 5090 GPUs. We follow

Prism (Tang et al., 2026) to conduct all experiments. We use LLaVA-v1.5-7B (Liu et al., 2023) as the backbone MLLM and employ the text tower of CLIP-L/14-336 (Radford et al., 2021) to extract instruction embeddings for semantic routing. We inject LoRA adapters into the attention projections of the LLM. Each task is trained for 1 epoch using the AdamW optimizer with a learning rate of 2×10^{-4} and a linear warm-up ratio of 0.03. A batch size of 8 is used across all benchmarks. For CRAM, hyperparameters are configured as follows: semantic routing margin $\theta = 0.1$, RBF kernel bandwidth $\sigma = 2$, spectral allocation threshold $\tau_{\text{alloc}} = 0.08$, and orthogonality filtering threshold $\tau_{\text{orth}} = 0.99$. For the warm-up stage in Sec. 4.2, we allocate 0.05 of training steps and initialize the rank of the temporary buffer \mathbf{W}_B to 48. All other implementation details are provided in Appendix C.

Evaluation Metrics. Following Zhou et al. (2024b); Chen et al. (2024), we report average final performance $\bar{\mathcal{A}} = \frac{1}{T} \sum_{s=1}^T \mathcal{A}_{s,T}$, where $\mathcal{A}_{s,T}$ denotes accuracy on task s after learning all T tasks.

5.2 Main Results.

We evaluate CRAM on the UCIT and TriGap (Tabs. 1, 2). On the 10-task TriGap benchmark, CRAM achieves an average accuracy of 47.79%, surpassing the strongest baseline DISCO by 1.25%. The consistent improvements across heterogeneous domains (e.g., 2.14% on ChemVQA) reveal that as the task stream lengthens, adaptive-rank instantiation effectively curbs parameter redundancy by allocating capacity only to unmet capability gaps, while orthogonality filtering ensures new ex-

Table 3: Component-wise Ablation.

Variant	Avg. Acc (%)
Baseline	53.31
w/ Group	66.38
w/ Group + Adaptive	68.92
w/ Group + Adaptive + Centroid (CRAM)	74.73

Table 4: Ablation on design choices.

Variant	Avg. Acc (%)
CRAM (Full)	74.73
Gaussian RBF \rightarrow cosine similarity	55.29
warm-up centroid init \rightarrow zero init	57.29

perts complement rather than overwrite established knowledge. On UCIT, CRAM attains 74.73%, substantially outperforming shared-adaptation baselines like MoE-LoRA by 13.94%. This directly validates the necessity of isolating instruction formats: by clustering semantically similar prompts, our routing mechanism neutralizes the gradient interference that typically degrades performance in unified parameter spaces.

5.3 Ablation Study

We conduct an ablation study on the UCIT benchmark. For variants without adaptive-rank instantiation, the rank is fixed to the average rank of the full CRAM to ensure parameter-aligned evaluation.

Component-wise Ablation. Tab. 3 details step-wise gains. **Baseline** denotes MoE-LoRA with a fixed expert rank of $r = 8$, deliberately aligned with CRAM’s average rank on UCIT (7.94) for parameter-equivalent comparison (In Tab. 1 MoE-LoRA use $r = 16$). *Group-isolated routing* (+13.07%) neutralizes format interference via semantic clustering. *Adaptive-rank instantiation* (+2.54%) targets capability gaps through orthogonality filtering, improving parameter efficiency. *Centroid-guided learning* (+5.81%) stabilizes expert activation and resolves aggregation imbalance via RBF routing and orthogonal constraints.

Design Choices. Tab. 4 validates key components via substitution with simpler alternatives. Replacing Gaussian RBF scoring with cosine similarity reduces accuracy by 19.44%, confirming that RBF’s distance-decay property is essential for stable expert activation. Replacing warm-up centroid initialization with zero initialization reduces performance by 17.44% due to off-manifold instability.

5.4 Further Analysis

Clustering Analysis. We visualize instruction embeddings using t-SNE (Van der Maaten and Hinton, 2008) to examine whether the learned groups re-

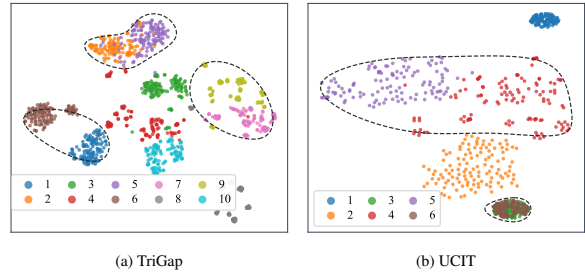


Figure 4: Visualization of instruction embeddings on TriGap (a) and UCIT (b). Circled regions indicate instructions assigned to the same group.

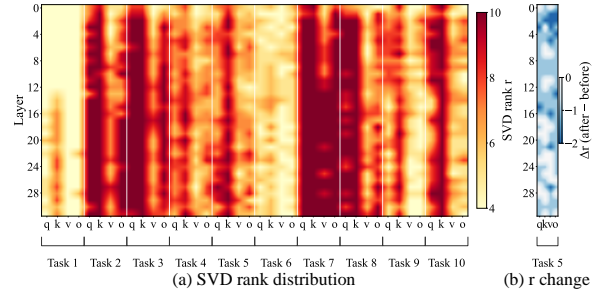


Figure 5: Adaptive rank allocation analysis. (a) Rank distribution across tasks, layers, and modules. (b) Effect of orthogonality filtering: rank allocation for task 5 before/after projecting out historical subspaces.

flect meaningful instruction structures. As shown in Fig. 4, clear clusters emerge across both benchmarks: PMCVA and ArxivQA (multiple-choice) form tight groups, confirming effective grouping. On TriGap, IconQA exhibits diffuse boundaries due to heterogeneous templates, where our relative-confidence margin prevents hard assignment in ambiguous cases, avoiding cross-format interference. This ensures shared adaptation occurs only for unambiguously aligned instructions.

Rank Allocation Analysis. To analyze how our method dynamically distributes parameter budgets, we examine the rank allocation across tasks and attention modules, as shown in Fig. 5(a). The results reveal three systematic patterns: (1) *Complexity-driven scaling*, where capacity correlates with task difficulty (e.g., Roadside receives high ranks, while InfographicVQA requires minimal parameters); (2) *Asymmetric module demands*, exhibiting a consistent $K > Q > O > V$ hierarchy across attention projections aligned with their functional roles; and (3) *Intra-cluster reuse*, where tasks within the same semantic cluster receive progressively lower ranks (e.g., Task 5 vs. Task 2), directly evidencing efficient knowledge transfer. This efficiency stems from the orthogonality filtering, which automatically discards parameter directions already mastered by historical experts. As illustrated in

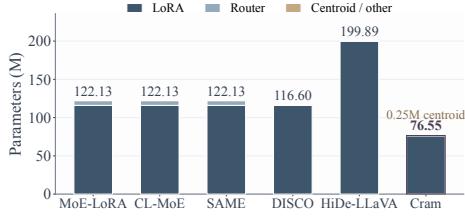


Figure 6: Parameter comparison on TriGap.

Table 5: Hyperparameter sensitivity on UCIT.

Param.	θ			σ			warm-up		
	0.08	0.10	0.15	1.0	2.0	3.0	0.03	0.05	0.10
Acc (%)	72.4	74.7	73.7	72.6	74.7	71.4	70.2	74.7	73.2

Fig. 5(b), the filtering predominantly prunes redundant components in lower-layer V/O projections, confirming that historical subspace overlap concentrates on input-proximal visual features. Consequently, CRAM preserves foundational representations while dedicating newly allocated capacity to higher-level reasoning pathways.

Parameter Efficiency. As shown in Fig. 6, by allocating parameters exclusively to capability gaps, CRAM achieves SOTA performance using the fewest parameters.

Hyperparameter Sensitivity. Achieving SOTA on both UCIT and TriGap with identical hyperparameters demonstrates strong cross-benchmark stability. Tab. 5 further shows that varying hyperparameters on UCIT yields only moderate fluctuations, confirming CRAM is robust to hyperparameter choices.

Format Interference and Instruction-Following Dynamics. To further probe how format heterogeneity interferes with sequential adaptation, we extend the single-step analysis from Fig. 1a into a multi-step continual setting, as shown in Fig. 7. (1) *Different instruction formats exhibit varying susceptibility* Strongly constrained conventions (e.g., *McqLetter* and *Yes/No*) degrade sharply when followed by heterogeneous tasks, whereas flexible formats (e.g., *Short*) show greater resilience. (2) *Does the model merely overfit to answer formats?* Evidence suggests otherwise. For tasks with aligned instruction understanding, such as *MCQLetter* and *MCQText*, they fundamentally share the core capability to extract correct answers. Consequently, training on *MCQLetter* effectively enhances instruction-following capability on *McqText*, significantly mitigating performance forgetting. However, this transfer pattern is inherently *asymmetric*: training on more permissive formats (e.g., *MCQText*) severely disrupts strict boundaries (e.g., *MCQLetter*), rather than yielding positive

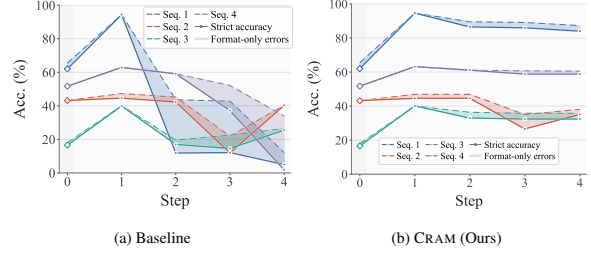


Figure 7: Sequential format adaptation. We construct four instruction-response conventions (**A**=MCQLetter (letter answer), **B**=MCQText (text answer), **C**=Short, **D**=Yes/No) from sampled data of ArxivQA by varying only the instruction-response format. For each training order (Seq. 1–4: ABCD/BCDA/CDAB/DABC), we evaluate the model on the first trained format after every step. *Strict accuracy* requires both format adherence and content correctness; *content-correct ceiling* counts format-violating but semantically correct responses.

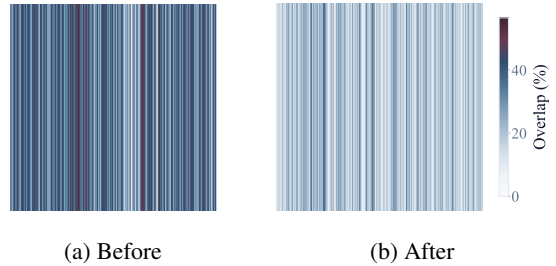


Figure 8: Overlap between ΔW and a historical expert before and after orthogonality filtering. Each column of ΔW is colored by its projection ratio onto the column space of a reference historical expert.

transfer. This confirms that while the model is genuinely acquiring instruction-following capabilities, its output behavior remains highly sensitive to surface format conventions. Rigid syntactic templates are thus highly vulnerable to *relaxation-induced drift*, which CRAM effectively mitigates by isolating format subspaces to sustain stable performance.

Overlap Analysis. Fig. 8 visualizes the column-wise subspace overlap between ΔW and a historical expert before and after orthogonality filtering. The average overlap drops from 36.5% to 18.1%, confirming that CRAM successfully removes components aligned with historical subspaces.

6 Conclusion

We propose CRAM, which mitigates catastrophic forgetting in MCIT by decoupling instruction isolation from visual adaptation. Through semantic grouping, adaptive instantiation, and centroid-routing, CRAM achieves superior retention and parameter efficiency on diverse benchmarks, offering a scalable solution for rehearsal-free MCIT.

Limitations

While CRAM demonstrates strong performance on current benchmarks, it has not yet been validated on significantly longer task sequences. Extending evaluation to larger-scale continual streams remains an important direction for future work.

References

- Jinze Bai, Shuai Bai, Shusheng Yang, Shijie Wang, Sinan Tan, Peng Wang, Junyang Lin, Chang Zhou, and Jingren Zhou. 2023. Qwen-vl: A versatile vision-language model for understanding, localization, text reading, and beyond. *arXiv preprint arXiv:2308.12966*.
- Meng Cao, Yuyang Liu, Yingfei Liu, Tiancai Wang, Jiahua Dong, Henghui Ding, Xiangyu Zhang, Ian Reid, and Xiaodan Liang. 2024. Continual llava: Continual instruction tuning in large vision-language models. *arXiv preprint arXiv:2411.02564*.
- Chang Che, Ziqi Wang, Pengwan Yang, Cheems Wang, Hui Ma, and Zenglin Shi. 2026. Lora in lora: Towards parameter-efficient architecture expansion for continual visual instruction tuning. In *Proceedings of the AAAI Conference on Artificial Intelligence*, pages 19978–19986.
- Cheng Chen, Junchen Zhu, Xu Luo, Heng T Shen, Jingkuan Song, and Lianli Gao. 2024. Coin: A benchmark of continual instruction tuning for multimodal large language models. *Advances in Neural Information Processing Systems*, pages 57817–57840.
- Jinpeng Chen, Runmin Cong, Yuzhi Zhao, Hongzheng Yang, Guangneng Hu, Horace Ip, and Sam Kwong. 2025. SEFE: Superficial and essential forgetting eliminator for multimodal continual instruction tuning. In *International Conference on Machine Learning*, pages 7982–8001.
- Chendi Ge, Xin Wang, Zeyang Zhang, Hong Chen, Jiapei Fan, Longtao Huang, Hui Xue, and Wenwu Zhu. 2025. Dynamic mixture of curriculum lora experts for continual multimodal instruction tuning. *arXiv preprint arXiv:2506.11672*.
- Runwei Guan, Rongsheng Hu, Shangshu Chen, Ningyuan Xiao, Xue Xia, Jiayang Liu, Beibei Chen, Ziren Tang, Ningwei Ouyang, Shaofeng Liang, and 1 others. 2026. Roadscenenvqa: Benchmarking visual question answering in roadside perception systems for intelligent transportation system. In *Proceedings of the AAAI Conference on Artificial Intelligence*, pages 4366–4375.
- Haiyang Guo, Fanhu Zeng, Ziwei Xiang, Fei Zhu, Da-Han Wang, Xu-Yao Zhang, and Cheng-Lin Liu. 2025a. Hide-llava: Hierarchical decoupling for continual instruction tuning of multimodal large language model. In *ACL*, pages 13572–13586.
- Haiyang Guo, Fanhu Zeng, Fei Zhu, Wenzhuo Liu, Da-Han Wang, Jian Xu, Xu-Yao Zhang, and Cheng-Lin Liu. 2025b. Federated continual instruction tuning. In *Proceedings of the IEEE international conference on computer vision*, pages 1325–1335.
- Haiyang Guo, Fei Zhu, Hongbo Zhao, Fanhu Zeng, Wenzhuo Liu, Shijie Ma, Da-Han Wang, and Xu-Yao Zhang. 2025c. Mcitlib: Multimodal continual instruction tuning library and benchmark. *arXiv preprint arXiv:2508.07307*.
- Danna Gurari, Qing Li, Abigale J Stangl, Anhong Guo, Chi Lin, Kristen Grauman, Jiebo Luo, and Jeffrey P Bigham. 2018. Vizwiz grand challenge: Answering visual questions from blind people. In *Proceedings of the IEEE/CVF Computer Vision and Pattern Recognition Conference*, pages 3608–3617.
- Dan Hendrycks, Steven Basart, Norman Mu, Saurav Kadavath, Frank Wang, Evan Dorundo, Rahul Desai, Tyler Zhu, Samyak Parajuli, Mike Guo, and 1 others. 2021. The many faces of robustness: A critical analysis of out-of-distribution generalization. In *Proceedings of the IEEE international conference on computer vision*, pages 8340–8349.
- Edward J Hu, Yelong Shen, Phillip Wallis, Zeyuan Allen-Zhu, Yuanzhi Li, Shean Wang, Lu Wang, Weizhu Chen, and 1 others. 2022. Lora: Low-rank adaptation of large language models. *ICLR*, 1(2):3.
- Tianyu Huai, Jie Zhou, Xingjiao Wu, Qin Chen, Qingchun Bai, Ze Zhou, and Liang He. 2025. Clmoe: Enhancing multimodal large language model with dual momentum mixture-of-experts for continual visual question answering. In *Proceedings of the IEEE/CVF Computer Vision and Pattern Recognition Conference*, pages 19608–19617.
- Yukang Huo and Hao Tang. 2025. When continue learning meets multimodal large language model: A survey. *arXiv preprint arXiv:2503.01887*.
- Ziqi Jia, Anmin Wang, Xiaoyang Qu, Xiaowen Yang, and Jianzong Wang. 2025. Hierarchical-task-aware multi-modal mixture of incremental lora experts for embodied continual learning. In *Proceedings of the Annual Meeting of the Association for Computational Linguistics*, pages 28415–28427.
- Kailin Jiang, Yuntao Du, Yukai Ding, Yuchen Ren, Ning Jiang, Zhi Gao, Zilong Zheng, Lei Liu, Bin Li, and Qing Li. 2026. When large multimodal models confront evolving knowledge: Challenges and explorations. In *International Conference on Learning Representations*.
- Hyundong Jin, Hyung Jin Chang, and Eunwoo Kim. 2025. Instruction-grounded visual projectors for continual learning of generative vision-language models. In *Proceedings of the IEEE/CVF International Conference on Computer Vision*, pages 3466–3476.
- Dongjun Kim, Seohyeon Cha, Huancheng Chen, Chining Wang, and Haris Vikalo. 2026. Quantized

- gradient projection for memory-efficient continual learning. In *International Conference on Learning Representations*.
- James Kirkpatrick, Razvan Pascanu, Neil Rabinowitz, Joel Veness, Guillaume Desjardins, Andrei A Rusu, Kieran Milan, John Quan, Tiago Ramalho, Agnieszka Grabska-Barwinska, and 1 others. 2017. Overcoming catastrophic forgetting in neural networks. *PNAS*, 114(13):3521–3526.
- Minjae Lee, Minhyuk Seo, Tingyu Qu, Tinne Tuytelaars, and Jonghyun Choi. 2025. Oasis: Online sample selection for continual visual instruction tuning. *arXiv preprint arXiv:2506.02011*.
- Lei Li, Yuqi Wang, Runxin Xu, Peiyi Wang, Xiachong Feng, Lingpeng Kong, and Qi Liu. 2024. Multimodal arxiv: A dataset for improving scientific comprehension of large vision-language models. In *Proceedings of the Annual Meeting of the Association for Computational Linguistics*, pages 14369–14387.
- Songze Li, Mingyu Gao, Tonghua Su, Xu-Yao Zhang, and Zhongjie Wang. 2025. Multimodal continual instruction tuning with dynamic gradient guidance. *arXiv preprint arXiv:2511.15164*.
- Adam Dahlgren Lindström and Savitha Sam Abraham. 2022. Clevr-math: A dataset for compositional language, visual and mathematical reasoning. *arXiv preprint arXiv:2208.05358*.
- Haotian Liu, Chunyuan Li, Qingyang Wu, and Yong Jae Lee. 2023. Visual instruction tuning. In *Advances in Neural Information Processing Systems*, pages 34892–34916.
- Wenzhuo Liu, Fei Zhu, Haiyang Guo, Longhui Wei, and Cheng-Lin Liu. 2025a. Llava-c: Continual improved visual instruction tuning. *arXiv preprint arXiv:2506.08666*.
- Yuyang Liu, Qiuhe Hong, Linlan Huang, Alexandra Gomez-Villa, Dipam Goswami, Xialei Liu, Joost van de Weijer, and Yonghong Tian. 2025b. Continual learning for vlms: A survey and taxonomy beyond forgetting. *arXiv preprint arXiv:2508.04227*.
- Pan Lu, Liang Qiu, Jiaqi Chen, Tony Xia, Yizhou Zhao, Wei Zhang, Zhou Yu, Xiaodan Liang, and Song-Chun Zhu. 2021. Iconqa: A new benchmark for abstract diagram understanding and visual language reasoning. *arXiv preprint arXiv:2110.13214*.
- Imad Eddine Marouf, Enzo Tartaglione, Stéphane Lathuilière, and Joost Van De Weijer. 2025. Ask and remember: A questions-only replay strategy for continual visual question answering. In *Proceedings of the IEEE/CVF International Conference on Computer Vision*, pages 18078–18089.
- Ahmed Masry, Xuan Long Do, Jia Qing Tan, Shafiq Joty, and Enamul Hoque. 2022. Chartqa: A benchmark for question answering about charts with visual and logical reasoning. In *Findings of the association for computational linguistics*, pages 2263–2279.
- Minesh Mathew, Viraj Bagal, Rubèn Tito, Dimosthenis Karatzas, Ernest Valveny, and CV Jawahar. 2022. Infographicvqa. In *Proceedings of the IEEE/CVF Winter Conference on Applications of Computer Vision*, pages 1697–1706.
- Minesh Mathew, Dimosthenis Karatzas, and CV Jawahar. 2021. Docvqa: A dataset for vqa on document images. In *Proceedings of the IEEE/CVF winter conference on applications of computer vision*, pages 2200–2209.
- Bryan A Plummer, Liwei Wang, Chris M Cervantes, Juan C Caicedo, Julia Hockenmaier, and Svetlana Lazebnik. 2015. Flickr30k entities: Collecting region-to-phrase correspondences for richer image-to-sentence models. In *Proceedings of the IEEE international conference on computer vision*, pages 2641–2649.
- Jingyang Qiao, Zhizhong Zhang, Xin Tan, Yanyun Qu, Shouhong Ding, and Yuan Xie. 2024. Large continual instruction assistant. *arXiv preprint arXiv:2410.10868*.
- Alec Radford, Jong Wook Kim, Chris Hallacy, Aditya Ramesh, Gabriel Goh, Sandhini Agarwal, Girish Sastry, Amanda Askell, Pamela Mishkin, Jack Clark, and 1 others. 2021. Learning transferable visual models from natural language supervision. In *International Conference on Machine Learning*, pages 8748–8763.
- Maryam Rahneemoonfar, Tashnim Chowdhury, Argho Sarkar, Debvrat Varshney, Masoud Yari, and Robin Roberson Murphy. 2021. Floodnet: A high resolution aerial imagery dataset for post flood scene understanding. *IEEE Access*, 9:89644–89654.
- Sylvestre-Alvise Rebuffi, Alexander Kolesnikov, Georg Sperl, and Christoph H Lampert. 2017. icarl: Incremental classifier and representation learning. In *Proceedings of the IEEE/CVF Computer Vision and Pattern Recognition Conference*, pages 2001–2010.
- Karsten Roth, Vishaal Udandarao, Sebastian Dziadzio, Ameya Prabhu, Mehdi Cherti, Oriol Vinyals, Olivier Hénaff, Samuel Albanie, Matthias Bethge, and Zeynep Akata. 2024. A practitioner’s guide to continual multimodal pretraining. *arXiv preprint arXiv:2408.14471*.
- María Virginia Sabando, Pavol Ulbrich, Matías Selzer, Jan Byška, Jan Mičan, Ignacio Ponzoni, Axel J Soto, María Luján Ganuza, and Barbora Kozlíková. 2020. Chemva: interactive visual analysis of chemical compound similarity in virtual screening. *IEEE Transactions on Visualization and Computer Graphics*, 27(2):891–901.
- Jun-Tao Tang, Yu-Cheng Shi, Zhen-Hao Xie, and Da-Wei Zhou. 2026. Prism: A plug-in reproducible infrastructure for scalable multimodal continual instruction tuning. *arXiv preprint arXiv:2605.26110*.
- Shengbang Tong, David Fan, Jiachen Li, Yunyang Xiong, Xinlei Chen, Koustuv Sinha, Michael Rabbat,

- Yann LeCun, Saining Xie, and Zhuang Liu. 2025. Metamorph: Multimodal understanding and generation via instruction tuning. In *Proceedings of the IEEE international conference on computer vision*, pages 17001–17012.
- Jianhong Tu, Zhuohao Ni, Nicholas Crispino, Zihao Yu, Michael Bendersky, Beliz Gunel, Ruoxi Jia, Xin Liu, Lingjuan Lyu, Dawn Song, and 1 others. 2025. Mlan: Language-based instruction tuning preserves and transfers knowledge in multimodal language models. In *Proceedings of the Workshop on Towards Knowledgeable Foundation Models (KnowFM)*, pages 59–74.
- Laurens Van der Maaten and Geoffrey Hinton. 2008. Visualizing data using t-sne. *Journal of machine learning research*, 9(11).
- Runyu Wang, Peng Ping, Zhengyu Guo, Xiaoye Zhang, Quan Shi, Liting Zhou, and Tianbo Ji. 2025a. Loki: Low-damage knowledge implanting of large language models. *arXiv preprint arXiv:2505.22120*.
- Xiao Wang, Tianze Chen, Qiming Ge, Han Xia, Rong Bao, Rui Zheng, Qi Zhang, Tao Gui, and Xuan-Jing Huang. 2023. Orthogonal subspace learning for language model continual learning. In *Findings of the Association for Computational Linguistics: EMNLP*, pages 10658–10671.
- Ziqi Wang, Chang Che, Qi Wang, Yangyang Li, Zenglin Shi, and Meng Wang. 2025b. Smolora: Exploring and defying dual catastrophic forgetting in continual visual instruction tuning. In *Proceedings of the IEEE international conference on computer vision*, pages 177–186.
- Ziqi Wang, Chang Che, Qi Wang, Hui Ma, Zenglin Shi, Cees GM Snoek, and Meng Wang. 2025c. Harmonious parameter adaptation in continual visual instruction tuning for safety-aligned mllms. *arXiv preprint arXiv:2511.20158*.
- Zhen-Hao Xie, Jun-Tao Tang, Yu-Cheng Shi, Han-Jia Ye, De-Chuan Zhan, and Da-Wei Zhou. 2026. Same: Stabilized mixture-of-experts for multimodal continual instruction tuning. *arXiv preprint arXiv:2602.01990*.
- Jieping Ye and Qi Li. 2005. A two-stage linear discriminant analysis via qr-decomposition. *IEEE Transactions on Pattern Analysis and Machine Intelligence*, 27(6):929–941.
- Yahan Yu, Duzhen Zhang, Yong Ren, Xuanle Zhao, Xiuyi Chen, and Chenhui Chu. 2025. Progressive lora for multimodal continual instruction tuning. In *ACL*, pages 2779–2796.
- Xiang Yue, Yuansheng Ni, Kai Zhang, Tianyu Zheng, Ruoqi Liu, Ge Zhang, Samuel Stevens, Dongfu Jiang, Weiming Ren, Yuxuan Sun, and 1 others. 2024. Mmmu: A massive multi-discipline multimodal understanding and reasoning benchmark for expert agi. In *Proceedings of the IEEE/CVF conference on computer vision and pattern recognition*, pages 9556–9567.
- Fanhu Zeng, Fei Zhu, Haiyang Guo, Xu-Yao Zhang, and Cheng-Lin Liu. 2025. Modalprompt: Towards efficient multimodal continual instruction tuning with dual-modality guided prompt. In *Proceedings of the Conference on Empirical Methods in Natural Language Processing*, pages 12137–12152.
- Shengyu Zhang, Linfeng Dong, Xiaoya Li, Sen Zhang, Xiaofei Sun, Shuhe Wang, Jiwei Li, Runyi Hu, Tianwei Zhang, Guoyin Wang, and 1 others. 2023a. Instruction tuning for large language models: A survey. *ACM Computing Surveys*.
- Xiaoman Zhang, Chaoyi Wu, Ziheng Zhao, Weixiong Lin, Ya Zhang, Yanfeng Wang, and Weidi Xie. 2023b. Pmc-vqa: Visual instruction tuning for medical visual question answering. *arXiv preprint arXiv:2305.10415*.
- Hengyuan Zhao, Ziqin Wang, Qixin Sun, Kaiyou Song, Yilin Li, Xiaolin Hu, Qingpei Guo, and Si Liu. 2025. Llava-cmoe: Towards continual mixture of experts for large vision-language models. *arXiv preprint arXiv:2503.21227*.
- Da-Wei Zhou, Hai-Long Sun, Jingyi Ning, Han-Jia Ye, and De-Chuan Zhan. 2024a. Continual learning with pre-trained models: a survey. In *IJCAI*, pages 8363–8371.
- Da-Wei Zhou, Qi-Wei Wang, Zhi-Hong Qi, Han-Jia Ye, De-Chuan Zhan, and Ziwei Liu. 2024b. Class-incremental learning: A survey. *IEEE Transactions on Pattern Analysis and Machine Intelligence*, 46(12):9851–9873.
- Deyao Zhu, Jun Chen, Xiaoqian Shen, Xiang Li, and Mohamed Elhoseiny. 2023. Minigpt-4: Enhancing vision-language understanding with advanced large language models. *arXiv preprint arXiv:2304.10592*.
- Zhen Zhu, Yiming Gong, Yao Xiao, Yaoyao Liu, and Derek Hoiem. 2025. How to teach large multimodal models new skills. *arXiv preprint arXiv:2510.08564*.

A Pseudocode

Algorithm 1 CRAM Training (per task t)

Require: \mathcal{D}_t ; frozen (ϕ, π, f, ψ) ; groups $\{\mathbf{c}_g\}$, pools $\{\mathcal{K}_g\}$
Ensure: New expert $(\mathbf{A}_t, \mathbf{B}_t)$ and centroid \mathbf{w}_t

- 1: **Level-1 routing.** $\mathbf{e} \leftarrow \psi(q)/\|\psi(q)\|_2$; assign g^* by Eq. (2)–(3)
- 2: Allocate expert slot k_t in \mathcal{K}_{g^*} ; init buffer \mathbf{W}_B
- 3: **Warm-up.** Train \mathbf{W}_B with \mathcal{L}_{NLL} (Eq. (1)); accumulate $\xi = \text{MeanPool}(\phi(v))$ to init \mathbf{w}_{k_t}
- 4: **Instantiation (SVD-Filter).**
- 5: Perform SVD: $\Delta \mathbf{W}_B = \mathbf{U}\Sigma\mathbf{V}^\top$ \triangleright Eq. (4)
- 6: Keep singular values $\sigma_p > \tau_{\text{alloc}}$
- 7: Build \mathbf{Q} from $[\mathbf{A}_1^\top, \mathbf{A}_2^\top, \dots]$; filter by α_p (Eq. (6))
- 8: Reconstruct $(\mathbf{A}_{k_t}, \mathbf{B}_{k_t})$ via Eq. (7)
- 9: **Stable training.**
- 10: $\omega_{i,k}$ from Eqs. (8)–(9); forward
- 11: Minimize $\mathcal{L} = \mathcal{L}_{\text{NLL}} + \mathcal{L}_{\text{dec}}$ (Eqs. (1), (10), (11))
- 12: Freeze $(\mathbf{A}_{k_t}, \mathbf{B}_{k_t}, \mathbf{w}_{k_t})$; reset \mathbf{W}_B

Algorithm 2 CRAM Inference

Require: Sample (v, q) ; frozen $\{\mathbf{c}_g\}$, $\{\mathcal{K}_g\}$, experts $\{(\mathbf{A}_k, \mathbf{B}_k)\}$, centroids $\{\mathbf{w}_k\}$
Ensure: Response \hat{y}

- 1: $\mathbf{e}(q) \leftarrow \psi(q)/\|\psi(q)\|_2$; $g^* \leftarrow \arg \max_g \frac{\mathbf{c}_g^\top \mathbf{e}(q)}{\|\mathbf{c}_g\|_2}$
- 2: $\xi \leftarrow \text{MeanPool}(\phi(v))$
- 3: $\omega_k \leftarrow \rho(\xi, \mathbf{w}_k) / \sum_{j \in \mathcal{K}_{g^*}} \rho(\xi, \mathbf{w}_j)$ \triangleright Eqs. (9)–(8)
- 4: $z \leftarrow [\pi(\phi(v)); \text{Emb}(q)]$; decode \hat{y}

B Experimental Details of Format Interference

To isolate the impact of instruction format heterogeneity, we design a controlled experiment using the ArxivQA (Li et al., 2024) dataset. The goal is to test whether training on a single output convention degrades performance on other conventions despite identical visual and semantic content.

B.1 Data Construction

The original ArxivQA samples are multiple-choice questions with four options. We start from the Letter format (the original format), where the model answers with a single letter. From this source, we generate three derived formats by programmatically converting the instruction and answer fields while keeping the image and the semantic correct answer unchanged.

Letter (McqLetter): The model outputs the option letter. Instruction ends with: “Answer with the option’s letter from the given choices directly.” Answer: a single letter, e.g., “B”.

Text (McqText): The model outputs the full text of the chosen option. Options are rewritten as “A. ...”, “B. ...”, etc. Instruction: “Choose the correct answer and reply with the full text of that choice, exactly as written among the options. Do not use the option letter.” Answer: the full option text, e.g., 10^{-1} Mpc^{-1} .

Short (Short): The model outputs a short answer (one or two words). Options are removed; the instruction asks for a concise answer. To control the difficulty and avoid overly long or complex answers, we retain only samples where the correct option text contains ≤ 2 tokens. Instruction: “Answer with the exact wording of the correct choice. The correct answer must be one or two words only; reply with those words only, no letters, punctuation, or extra explanation.” Answer: the short text, e.g., “0.48”.

Yes/No (YesNo): The model outputs “yes” or “no”. Two numbered statements (the correct option and a distractor) are presented, exactly one of which is correct. The order is randomly shuffled per sample. To control the difficulty and align with the semantic complexity of the other three formats, we avoid simple true/false questions that directly ask whether a single claim is correct. Instead, this two-statement comparison design requires the model to identify the correct option, ensuring that format conventions rather than answer triviality remain the primary controlled variable. Instruction: “Two numbered statements are given about the same question. Exactly one is correct. If statement (1) is correct, reply with exactly: yes. If statement (2) is correct, reply with exactly: no.” Answer: “yes” or “no”.

After conversion, we align the training and test set sizes across all four formats. For the Short format, the token-length filter (only retaining samples where the correct option text contains at most two tokens) inevitably reduces the number of usable samples. Therefore, we take the intersection of samples that survive this filter and the corresponding samples in the other three formats, ensuring

that all four variants are evaluated on exactly the same set of underlying questions.

B.2 Training and Evaluation Protocol

For each format $f \in \{\text{Letter, Text, Short, Yes/No}\}$, we perform parameter-efficient fine-tuning (PEFT) by inserting LoRA adapters of rank $r = 8$ into the attention layers (i.e., $q_proj, v_proj, k_proj, o_proj$) of LLaVA-v1.5-7B. During training, only the LoRA parameters are learnable; the backbone MLLM remains frozen. The model is trained on the training set of that format for one epoch using the standard language modeling loss. After training, we evaluate the model on the test sets of *all four* formats, yielding a 4×4 accuracy matrix. The zero-shot baseline (LLaVA-v1.5-7B without fine-tuning) is also evaluated on all four test sets.

B.3 Error Analysis: Format-Wrong Content-Correct (FWCC)

To distinguish semantic forgetting from pure format violation, we define a sample as *format-wrong but content-correct* (FWCC) if the predicted answer is semantically equivalent to the ground truth but does not adhere to the required output convention of the test format. For each test format, we use a dedicated evaluator that first checks format compliance (e.g., single letter for Letter, exactly “yes”/“no” for Yes/No) and, if violated, attempts to extract the semantic content using rules (e.g., mapping option letters to option texts, normalizing case). The FWCC ratio is the proportion of incorrect predictions that are semantically correct but format-violating.

B.4 Correspondence with Main Paper Figures

The results are summarised in Fig. 1 in the main paper. Fig. 1(a) shows the accuracy change relative to zero-shot for each train–test format pair. The diagonal entries (training and testing on the same format) all achieve high accuracy, confirming that each format is learnable in isolation. However, the off-diagonal entries reveal severe degradation: training on any single format leads to a substantial drop in accuracy when testing on other formats, even though the underlying visual and semantic content remain identical. This indicates that the model learns format-specific surface patterns that do not transfer across conventions.

Fig. 1(b) further reports the FWCC (Format-Wrong Content-Correct) ratio among errors. A high FWCC ratio indicates that the model still

Table 6: Implementation details.

Method	Insertion	Epoch	Config. (UCIT/TriGap)
FT-LoRA	Attn+FFN	1	96/80 (rank)
Replay-LoRA	Attn+FFN	1	96/80 (rank)
HiDe-LLaVA	Attn+FFN (N exp.)	1	16/8 (rank)
CL-MoE	FFN (N exp.)	1	16/8 (rank)
DiSCO	FFN (N exp.)	1	16/8 (rank)
ModalPrompt	Soft prompts ($\ell = 10$)	4	10 (prefix)
MoE-LoRA	FFN (N exp.)	1	16/8 (rank)
CRAM (Ours)	Attn (N exp.)	1	7.94/7.63 (rank)

retrieves the correct semantic answer but fails to adhere to the required output convention of the test format. Together, these two panels confirm that heterogeneous instruction formats inherently trigger severe interference, acting as a primary driver of catastrophic forgetting in shared-parameter regimes. Importantly, this interference stems from format-surface misalignment rather than loss of task semantics.

C Implementation details

For MoE-based baselines (HiDe-LLaVA, CL-MoE, DiSCO, MoELoRA), the reported rank is the per-expert average: total rank r is divided by the number of tasks N (UCIT: $N = 6$, TriGap: $N = 10$). For CRAM, the adaptive allocation mechanism dynamically determines the per-expert rank, resulting in the reported average values (7.94 for UCIT, 7.63 for TriGap). All methods inject adapters into the attention (Attn) or feed-forward network (FFN) layers as indicated. ModalPrompt uses soft prompts of length $\ell = 10$ instead of low-rank adapters.

D Geometric Properties of the Orthogonality Score

Let \mathbf{Q} be an orthonormal basis for the historical subspace $\mathcal{V}_{\text{hist}} = \text{col}(\mathbf{M}_{\text{hist}})$, so $\mathbf{Q}^\top \mathbf{Q} = \mathbf{I}_{R_{\text{hist}}}$. Define

$$\begin{aligned} \mathbf{P} &= \mathbf{Q}\mathbf{Q}^\top && (\text{onto } \mathcal{V}_{\text{hist}}), \\ \mathbf{P}_\perp &= \mathbf{I} - \mathbf{Q}\mathbf{Q}^\top && (\text{onto } \mathcal{V}_{\text{hist}}^\perp). \end{aligned}$$

Both are symmetric, idempotent, and satisfy $\mathbf{P}\mathbf{P}_\perp = \mathbf{0}$.

For a candidate SVD direction $\mathbf{v}_p \in \mathbb{R}^d$, the orthogonality score is

$$\alpha_p = \frac{\|\mathbf{P}_\perp \mathbf{v}_p\|_2}{\|\mathbf{v}_p\|_2} = \frac{\|(\mathbf{I} - \mathbf{Q}\mathbf{Q}^\top) \mathbf{v}_p\|_2}{\|\mathbf{v}_p\|_2}. \quad (12)$$

Proposition 1 (Bounds and Energy Interpretation). $\alpha_p \in [0, 1]$. $\alpha_p = 0$ iff $\mathbf{v}_p \in \mathcal{V}_{\text{hist}}$ (*fully redundant*); $\alpha_p = 1$ iff $\mathbf{v}_p \perp \mathcal{V}_{\text{hist}}$ (*fully novel*). Moreover, α_p^2 equals the fraction of $\|\mathbf{v}_p\|_2^2$ lying in $\mathcal{V}_{\text{hist}}^\perp$.

Proof. Decompose $\mathbf{v}_p = \mathbf{P}\mathbf{v}_p + \mathbf{P}_\perp\mathbf{v}_p = \mathbf{v}_p^\parallel + \mathbf{v}_p^\perp$. Since $\langle \mathbf{v}_p^\parallel, \mathbf{v}_p^\perp \rangle = 0$,

$$\|\mathbf{v}_p\|_2^2 = \|\mathbf{v}_p^\parallel\|_2^2 + \|\mathbf{v}_p^\perp\|_2^2. \quad (13)$$

Dividing by $\|\mathbf{v}_p\|_2^2 \neq 0$ yields $1 = \|\mathbf{v}_p^\parallel\|_2^2 / \|\mathbf{v}_p\|_2^2 + \alpha_p^2$, hence $0 \leq \alpha_p \leq 1$. Boundary cases: $\alpha_p = 0$ iff $\mathbf{v}_p^\perp = \mathbf{0}$, i.e. $\mathbf{v}_p \in \text{col}(\mathbf{Q})$; $\alpha_p = 1$ iff $\mathbf{v}_p^\parallel = \mathbf{0}$, i.e. $\mathbf{v}_p \perp \text{col}(\mathbf{Q})$. Finally, $\alpha_p^2 = \|\mathbf{v}_p^\perp\|_2^2 / \|\mathbf{v}_p\|_2^2$ measures the energy fraction in $\mathcal{V}_{\text{hist}}^\perp$. Thresholding by τ_{orth} retains only directions with $\alpha_p > \tau_{\text{orth}}$, so at least τ_{orth}^2 of their energy lies outside the historical subspace. \square

E Gradient Dynamics of the Decoupling Loss

The decoupling loss penalizes the new expert’s response to historical input directions:

$$\mathcal{L}_{\text{dec}} = \frac{1}{B} \sum_{i=1}^B \gamma_i \|\Delta\mathbf{W}_{\text{new}}(\mathbf{Q}\mathbf{Q}^\top \mathbf{h}_i)\|_2^2, \quad (14)$$

where $\gamma_i = \sum_{k \in \mathcal{K}_{g^*}} \omega_{i,k}$ measures reliance on historical experts and $\mathbf{h}_i \in \mathbb{R}^d$ are the input hidden states. Let $\tilde{\mathbf{h}}_i = \mathbf{Q}\mathbf{Q}^\top \mathbf{h}_i$, so $\mathcal{L}_{\text{dec}} = \frac{1}{B} \sum_{i=1}^B \gamma_i \|\Delta\mathbf{W}_{\text{new}} \tilde{\mathbf{h}}_i\|_2^2$.

Proposition 2 (Gradient Structure). *The gradient $\nabla_{\Delta\mathbf{W}_{\text{new}}} \mathcal{L}_{\text{dec}}$ is right-multiplied by $\mathbf{Q}\mathbf{Q}^\top$, so gradient descent suppresses $\Delta\mathbf{W}_{\text{new}}$ on historical input directions.*

Proof. From $\frac{\partial}{\partial \mathbf{X}} \|\mathbf{X}\mathbf{y}\|_2^2 = 2\mathbf{X}\mathbf{y}\mathbf{y}^\top$,

$$\begin{aligned} \frac{\partial \mathcal{L}_{\text{dec}}}{\partial \Delta\mathbf{W}_{\text{new}}} &= \frac{2}{B} \sum_{i=1}^B \gamma_i (\Delta\mathbf{W}_{\text{new}} \tilde{\mathbf{h}}_i) \tilde{\mathbf{h}}_i^\top \\ &= \frac{2}{B} \sum_{i=1}^B \gamma_i (\Delta\mathbf{W}_{\text{new}} \mathbf{Q}\mathbf{Q}^\top \mathbf{h}_i) \mathbf{h}_i^\top \mathbf{Q}\mathbf{Q}^\top. \end{aligned} \quad (15)$$

Thus, the gradient takes the form $\mathbf{G}\mathbf{Q}\mathbf{Q}^\top$ with $\mathbf{G} \in \mathbb{R}^{m \times d}$. The gradient descent update $\Delta\mathbf{W}_{\text{new}} \leftarrow \Delta\mathbf{W}_{\text{new}} - \eta \mathbf{G}\mathbf{Q}\mathbf{Q}^\top$ modifies only the components of $\Delta\mathbf{W}_{\text{new}}$ that map inputs from the historical subspace $\text{col}(\mathbf{Q})$. Minimizing \mathcal{L}_{dec} drives $\Delta\mathbf{W}_{\text{new}}\mathbf{Q} \rightarrow \mathbf{0}$, forcing near-zero outputs for historical directions. \mathcal{L}_{dec} acts as a soft regularizer alongside \mathcal{L}_{NLL} , penalizing redundant activations without enforcing hard orthogonality. \square

Table 7: Task-order robustness of **CRAM** on **UCIT**. We report average accuracy (%) under three task sequences: *Original* (benchmark-default order), *Reverse* (fully inverted order), and *Random* (fixed permutation for reproducibility).

CRAM (Ours)	Original	Reverse	Random
Avg. Accuracy (%)	74.73	73.06	72.89

Table 8: Task-order robustness of **CRAM** on **TriGap**. Settings follow Tab. 7: *Original*, *Reverse*, and *Random* denote the same task-order configurations.

CRAM (Ours)	Original	Reverse	Random
Avg. Accuracy (%)	47.79	46.97	48.01

F Robustness to Task Order

While Fig. 7b demonstrates CRAM’s stability under different sequential format adaptation, we further evaluate its robustness to task ordering on both UCIT and TriGap benchmarks. Specifically, for each benchmark we report results under three distinct task sequences:

- **Original:** the canonical task order as defined in the benchmark protocol;
- **Reverse:** the exact reverse of the original sequence (last task becomes first);
- **Random:** a randomly shuffled order. For reproducibility, we fix the random permutation to the following sequences:

UCIT: Flickr30k \rightarrow CLEVER \rightarrow ArxivQA \rightarrow ImageNet-R \rightarrow IconQA \rightarrow Vizcap

TriGap: ChemVQA \rightarrow CLEVR \rightarrow PMCVQA \rightarrow InfographicVQA \rightarrow Roadside \rightarrow DocVQA \rightarrow ArxivQA \rightarrow FloodNetVQA \rightarrow ChartQA \rightarrow IconQA

As shown in Tabs. 7 and 8, CRAM exhibits strong robustness to task ordering: performance fluctuations remain marginal across all sequences. This stability stems from two key designs: (1) *group-isolated routing* decouples format-level interference at the semantic level, making expert activation insensitive to the chronological arrival of tasks; and (2) *centroid-guided orthogonal learning* confines new updates to subspaces orthogonal to historical knowledge, preventing order-dependent accumulation of redundant directions. Notably, the minimal degradation under perturbed orders suggests that CRAM does not rely on a favorable task curriculum, making it suitable for realistic open-world deployment.

Table 9: OOD Generalization evaluated on MMMU.

Method	Art	Bus.	Sci.	H&M	Hum.	T&E	Avg
Zero-Shot	43.85	25.35	23.74	32.93	48.47	28.16	33.75
CRAM (Ours)	44.51	26.19	25.93	33.76	47.34	33.96	35.28

G OOD Generalization.

Tab. 9 evaluates cross-benchmark transfer by testing UCIT-trained models on MMMU (Yue et al., 2024), a diverse benchmark covering six domains: Art, Business, Science, Health & Medicine, Humanities, and Tech & Engineering. CRAM achieves higher average accuracy (+1.53% over zero-shot), outperforming the baseline in 5 out of 6 domains and matching it in the remaining one (Humanities). This consistent improvement suggests that CRAM not only mitigates catastrophic forgetting on the original tasks but also preserves task-agnostic visual representations that generalize to unseen domains.

The most notable gains appear in **Tech & Engineering** (+5.80%) and **Science** (+2.19%), which demand structured reasoning and domain-specific visual understanding. These tasks require the model to interpret technical diagrams, charts, and scientific figures, capabilities that are particularly vulnerable to overfitting under standard continual learning. By neutralizing format interference via semantic grouping and confining updates to orthogonal subspaces via orthogonal filtering, CRAM prevents the model from over-specializing to the UCIT training distribution. In contrast, domains with smaller gains (e.g., Business, +0.84%) or slight degradation (Humanities, -1.13%) rely more on general world knowledge or linguistic reasoning, where the baseline already maintains reasonable zero-shot performance and the room for improvement is limited.

These results demonstrate that CRAM’s design, including group-isolated routing, adaptive-rank instantiation, and centroid-guided orthogonal learning, effectively preserves transferable visual competencies while acquiring task-specific knowledge. The model does not simply memorize UCIT patterns but learns representations that generalize robustly to out-of-distribution benchmarks.

H Training Efficiency Analysis

Fig. 9 compares the training time of CRAM against the MoE-LoRA baseline across the six tasks of UCIT. While CRAM introduces additional computations due to warm-up SVD decomposition and or-

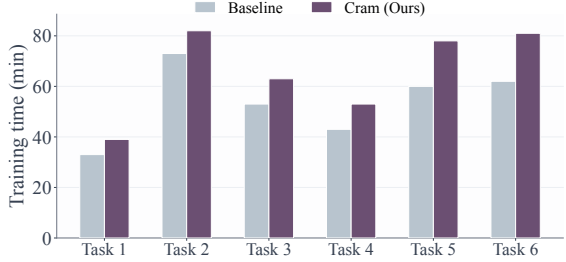


Figure 9: Training time comparison between Baseline (MoE-LoRA) and CRAM on UCIT.

Table 10: UCIT benchmark.

Dataset	Domain	Train	Test
ImageNet-R	Artistic	24,000	3,000
ArxivQA	Academic figures	40,000	3,000
VizWiz	Visual assistance	40,000	3,000
IconQA	Icons	30,000	3,000
CLEVR-Math	Synthetic reasoning	40,000	3,000
Flickr30k	Captioning	40,000	3,000

thogonal filtering, the training time increases only marginally compared to the baseline, incurring a modest overhead. This slight increase is well justified by substantial performance gains and enhanced parameter efficiency. Moreover, the overhead per task remains stable, as the adaptive-rank mechanism only activates during expert instantiation and does not accumulate across tasks. These results demonstrate that CRAM achieves superior continual instruction tuning performance with only a negligible training time penalty.

I Dataset Details

Tables 10 and 11 summarise the dataset splits for the UCIT and TriGap benchmarks. For each task, we report the training set size, test set size, and a brief domain description to illustrate the diversity of visual domains and instruction formats encountered during continual learning.

J Comprehensive Study on MCIT Methods

In this section, we provide details of the methods compared in the main paper. The specifics of each compared method are outlined as follows:

- **Replay-LoRA:** A rehearsal-based baseline that integrates a fixed-size episodic memory buffer with LoRA fine-tuning. During each

Table 11: TriGap benchmark.

Dataset	Domain	Train	Test
PMCVQA	Medical	40,000	3,000
DocVQA	Documents	30,000	3,000
ChartQA	Charts	25,000	3,000
IconQA	Icons	10,000	3,000
InfographicVQA	Infographics	20,000	3,000
ArxivQA	Academic figures	10,000	3,000
Roadside	Autonomous driving	40,000	3,000
ChemVQA	Molecules	40,000	3,000
FloodNetVQA	Disaster scenes	10,000	3,000
CLEVR	Synthetic reasoning	10,000	3,000

incremental task, it stores a representative subset of historical multimodal instructions and jointly optimizes the low-rank adapters using both current and replayed samples. This explicit data rehearsal strategy effectively constrains parameter drift and mitigates catastrophic forgetting while preserving parameter efficiency.

- MoELoRA:** This method extends LoRA-based fine-tuning to a Mixture-of-Experts architecture for continual instruction tuning, where each task activates a subset of LoRA experts via a learnable router, enabling parameter-efficient adaptation across sequential tasks without rehearsal. However, it remains vulnerable to router drift and expert drift as tasks accumulate.
- HiDe-LLaVA:** Based on CKA similarity analysis revealing distinct representation patterns between top and lower transformer layers, this method hierarchically decouples model adaptation: the top layer undergoes task-specific LoRA expansion with dual-modality anchor matching for expert selection, while lower layers fuse LoRAs across tasks to preserve general knowledge without router training.
- ModalPrompt:** A prompt-based framework that constructs task-specific prompts and leverages dual-modality guidance for two purposes: prompt fusion during training to transfer knowledge from semantically similar tasks, and prompt selection during inference to control computational complexity. The method maintains inference efficiency by selecting only k relevant prompts from a shared pool regardless of task count.
- CL-MoE:** A dual momentum Mixture-of-Experts framework designed for continual MLLM adaptation. It introduces a Dual-Router MoE (RMoE) that jointly employs task-level and instance-level routers to robustly allocate global and local experts. Coupled with a Dynamic Momentum MoE (MMoE), it categorizes experts into task-shared and task-specific types and dynamically updates their parameters via a momentum-based interpolation between historical and current knowledge. This mechanism effectively alleviates catastrophic forgetting and enhances both forward and backward transfer without relying on replay buffers.
- SAME:** SAME stabilizes MoE adaptation via spectral-aware routing (decomposing router updates into task-relevant and history-preserving subspaces) and curvature-aware scaling (regulating expert updates using historical input covariance). It also introduces adaptive expert activation to freeze selected experts during training, reducing redundant computation and cross-task interference. SAME achieves strong performance on MCIT benchmarks and serves as a direct point of comparison for our CRAM framework.
- DISCO:** A federated continual learning framework for LMMs that employs dynamic knowledge organization (DKO) to store task-specific parameters in a global cache using identity token matching, and subspace selective activation (SSA) to filter irrelevant outputs during inference. While originally designed for federated settings, its continual learning components are applicable to centralized MCIT and are included for comparison.